IEEE Access
Multidisciplinary | Rapid Review | Open Access Journal

Received October 18, 2018, accepted November 4, 2018, date of publication November 19, 2018,
date of current version December 18, 2018.

Digital Object Identifier 10.1109/ACCESS.2018.2881962

Steel Surface Defect Classification Based on Discriminant Manifold Regularized Local Descriptor

JIULIANG ZHAO[1], YISHU PENG[2], AND YUNHUI YAN[1]
[1]School of Mechanical Engineering and Automation, Northeastern University, Shenyang 110189, China
[2]School of Mechanical Engineering, Hunan Institute of Science and Technology, Yueyang 414600, China

Corresponding author: Yishu Peng (yishu_peng@126.com)

This work was supported in part by the National Key Research and Development Program of China under Grant 2017YFB0304200, in part by the National Natural Science Foundation (NNSF) under Grant 51374063, and in part by the Fundamental Research Funds for the Central Universities under Grant N150308001.

ABSTRACT Steel surface demonstrates various sorts of defects due to the production technique and environment. The appearance of defect is in much more random pattern than that of the normal texture image. Therefore, it is challenging to capture the discriminant information to categorize the defects. The defect image is out of image registration in grayscale, and thus, the local descriptor is inclined to be utilized for feature extraction. In the previous works, involving a local descriptor for categorizing the defect images, the thresholding operator participates in the hand-crafted feature extraction, such as local binary patterns and histogram of oriented gradient, leading to sub-optimal features. By introducing the learning mechanism into the construction of local descriptor, a novel algorithm named discriminant manifold regularized local descriptor (DMRLD) is proposed to conduct the defect classification task in this paper. First, the DMRLD computes the dense pixel difference vector (DPDV) to draw the local information of defect images. Then, the manifold of these DPDVs can be constructed by searching for a number of linear models to represent the feature. In order to enhance the discriminant ability of the feature, a projection on the manifold is learned for achieving a low-dimensional subspace. Finally, the manifold distance defined in the subspace can accomplish the matching task to get the category of the defect image. The proposed algorithm is first applied on the Kylberg texture dataset to evaluate the texture feature extraction performance, and then the experiments on the real steel surface defect dataset are conducted to illustrate the effectiveness of DMRLD compared with other local descriptors.

INDEX TERMS Steel surface defect classification, local descriptor, discriminant manifold learning, manifold metric.

I. INTRODUCTION

Steel is applied as the raw material in aerospace, automobile manufacturing, and power energy. With the high requirement of surface quality, steel surface defect classification plays an important role during the production. Due to the influences of material, rolling equipment, and the process craft, the quality of steel may degrade heavily. As a result, the steel surface appears sorts of defects, such as rolled-in scale, inclusion, and scratches. In the production process, it is necessary to capture the information of defects to avoid of defective products in the market. For this purpose, the defect inspection system (DIS) which devotes to controlling and improving the quality grade of steel products for steel surface has been widely used in steel industry [1]–[5].

Generally, the framework of DIS [6] which is visualized in Fig. 1 consists of two subsystems: image acquisition subsystem and processing subsystem. The two subsystems are connected via the system cabinet. The surface sensor captures the image data by employing the light and camera equipment. The inspection terminal handles the data and controls the system by transporting the user's requirement. Normally, the processing subsystem includes the computational server and the host computer to analyze the image data and report the real-time result. Given the image acquisition subsystem, the main mission lies in the processing subsystem which is the core of this paper as well.

The commonly-used techniques in the DIS employ the image processing and pattern recognition algorithms to

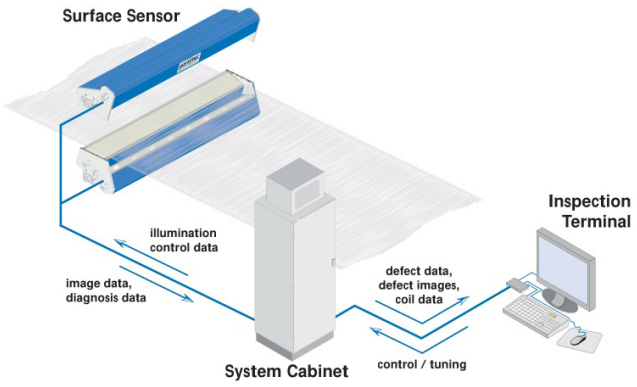

FIGURE 1. Procedure of the defect inspection system.

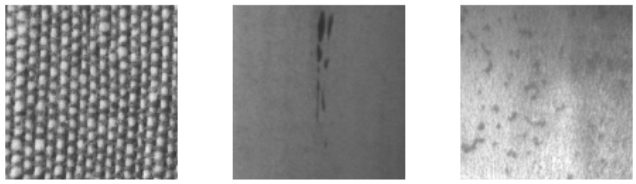

FIGURE 2. Example texture images: (a) normal texture image on the Kylberg dataset, (b) inclusion defect surface of the steel strip, and (c) pitted defect surface of the steel strip.

extract the feature of the defect target, and then categorize the feature into the given attribution of the defects. Different from the natural object image classification [7], [8], steel surface defect image classification is more challenging due to its random pattern. In recent years, there have been various researches for steel surface defect classification. Most of the related works on the feature extraction. Lee *et al.* [9] developed a feature extraction method to explore the textural characteristics of the defects and employed four classical entropy features in the spatial domain. As a result, the neural network was adopted to classify the features. Dongyan *et al.* [10] employed the multi-kernel function RVM which is solved by SOCP algorithm to improve the performance of defect classification recognition on steel strip surface. For the large scale steel surface defect dataset, Chu *et al.* [11] proposed a novel classification method based on enhanced twin support vector machine and binary tree to obtain the high classification accuracy and efficiency. Singhka *et al.* proposed artificial neural network based methodology to classify the various types of defects, such as blister, scratch and water droplet. Hu *et al.* [4] applied the hybrid chromosome genetic algorithm to establish the real-time defect detection and classification system. After the preprocessing, four sorts of features were extracted and the genetic algorithm was adopted to optimize the classification model. Experiments on the large-scale defect collection demonstrated the performance. Support vector machine is an effective classifier and has been used widely in classification applications, especially in surface defect classification [12]–[16]. Recently, Chu *et al.* [17] employ an improved support vector machine which uses multi-type statistical features for steel surface defect classification and achieve the promising results.

As one sort of the texture, the defect image presents a more random pattern than other sorts of texture images. In the defect image, the pixels are mainly divided into three categories: defect, background, and noise. The attribution of the defect is determined by combining the information of edge, shape and the reflection of the material. However, the pixels of the normal texture image group in a fixed pattern and repeat the pattern in the image, e.g. Fig. 2 (a), while the defect may present as an isolated target (Fig. 2 (b)) or repeat in the image (Fig. 2 (c)). Therefore, the feature of the defect image is much more challenging than that of the normal texture images. Based on the generation of the steel production, the background is beneficial to describe the distinguishable feature as well. It is vital to represent the defect in an optimal way to keep the balance between the background and defect target during the feature extraction. Another special part of the defect image lies in that the global structure is inconsistent with the local structure. Only with the local patch, it is difficult to determine the attribution of the defect even it works for the normal texture image.

Compared with the previous classification task which treats the aligned images, the texture images are without registration in most cases. Therefore, the local information is inclined to be utilized for generating the feature. In recent decades, there have been numerous local descriptors and the corresponding variants, such as local binary pattern (LBP) [18], histogram of oriented gradient (HOG) [19], and scale-invariant feature transform (SIFT) [20]. However, these hand-crafted descriptors introduce the thresholding operator which is sub-optimal for feature extraction. In addition, these local descriptors are independent of the classifier construction processing. Based on the properties of the local descriptors aforementioned, there are some issues of these descriptors for the steel surface defect image:

- LBP encodes the pixel with a real value by using the spatial neighborhoods, and then constructs the histogram of the defect image. The number of the defect pixels existing in the image is changeable, and the edge and shape cannot repeat frequently like the normal texture images. Thus, the histogram may loss the discriminant information of the defect image.
- HOG introduces the local information by encoding the local region of the image using an oriented histogram and concatenating these sub histograms to obtain the final feature. Compared with LBP, HOG prefers to extracting the edge information and taking into account the structure information of the image. However, HOG usually suffers from the problem of high dimension and ignoring the texture information. The raw information of the defect images are without registration, therefore, the structured HOG may be out of work for extracting the distinguishable feature of the defect images.

TABLE 1. Notations used in this paper.

Notation	Description
$X = \{x_1, x_2, \cdots, x_i, \cdots, x_n\} \in R^{L\times n}$	The collection of the DPDVs, where L is the length of the DPDV, n is the number of DPDVs in the image, and x_i denotes the i-th DPDV.
$W = \{W_{i,j}\}_{i=1,2,\cdots,c_m}^{j=1,2,\cdots,c_n}$	The affinity matrix which measure relation between the local model $C_{i,m}$ and $C_{j,n}$, where c_m and c_n are the number of DPDVs in the local models $C_{i,m}$ and $C_{j,n}$, respectively.
$\mathcal{M}_i = \{C_{i,1}, C_{i,2}, \cdots, C_{i,m}\}$	The i-th manifold consists of m local models.
$C_i = \{x_1^{(i)}, x_2^{(i)}, \cdots, x_{n_i}^{(i)}\}$	The i-th local model consists of n_i DPDVs.
S_w, S_b	The within-class and between-class scatter matrix.

- Compared with LBP and HOG, SIFT is totally a local descriptor which encodes the key point of the image using the histogram of gradient. SIFT achieves more useful and discriminant feature than LBP to measure the distinguishable feature of the defects. However, SIFT has a high requirement of the quality of the image. In the applications of the steel surface defect classification, the image may be out of the base requirement and cannot generate enough key points to supporting the SIFT descriptors.

As discussed above, the local descriptor cannot rely on the prior processing heavily. Besides, the local descriptor should assist in representing the distinguishable character of the image, preserving the principle component and decreasing the redundant information possibly. For this, this work proposes an algorithm named discriminant manifold regularized local descriptor (DMDL) to address the problem of steel surface defect classification. The proposed DMRLD measures the feature of the defect image using the manifold structure derived from the dense pixel difference vector (DPDV), and then transforms the defect classification task into the manifold construction and matching problem. Different from the previous algorithms of the local descriptor, the proposed DMRLD represents the image using the structure of manifold with learning mechanism rather than the histogram by the hand-crafted construction. Furthermore, the discriminant projection is employed to map the original manifold into the low-dimensional, discriminant subspace to improve the classification result.

The highlights of this work are mainly summarized as follows:

1) The feature of steel surface defect image is represented using the manifold regularized local descriptor via learning mechanism. The DPDVs of the image are utilized to construct the manifold whose function is equivalent to the histogram aforementioned.
2) The manifold distance is defined using the fused variation based and exemplar based distances for the defect images.
3) Discriminant analysis is conducted on the manifold to achieve the low-dimensional, discriminant subspace for extracting the distinguishable feature of the defect images.

The rest of this paper is organized as follows: Section 2 briefly introduces the related work; the proposed DMRLD algorithm for steel surface defect classification is presented in Sec. 3, and the experiments are conducted in Sec. 4. Section 5 concludes this paper in the end.

II. RELATED WORK

Since this work mainly discusses the local descriptor and involves the structure of manifold, the related work will be expanded around the previous works about the two points. Before introducing the related work, the notations and the corresponding descriptions used in this paper are declared in Table 1.

A. LOCAL DESCRIPTOR

As aforementioned, the local descriptor of the image can represent the global feature without the requirement of registration. Therefore, the local descriptor is beneficial to capture the distinguishable feature compared with that made of the raw gray value. As one of the representative local descriptor, the scheme of LBP is introduced in this subsection. LBP has been used in face recognition successfully due to its effectiveness [21]–[23]. There are two steps for generating the LBP feature descriptor. First, LBP computes the difference between the central pixel and its neighbors in the local sphere, such as a square window. Meanwhile, the difference is binarized using a fixed threshold, zero in general. Next, these binary bins of the central pixel are encoded as a decimal value in hand-crafted fashion. The whole processing of LBP descriptor is illustrated in Fig. 3. It is worth noting that the radius setting decides the number of binary bins and the length of LBP feature descriptor in further. From the construction of LBP feature descriptor, it can be observed that the key step of LBP is defined in hand-crafted fashion. For one thing, the encoding of the pixel is determined using a fixed threshold. For another, the number of bins, which is equivalent to the size of the codebook, is defined artificially as well. Due to the description of the local information, LBP

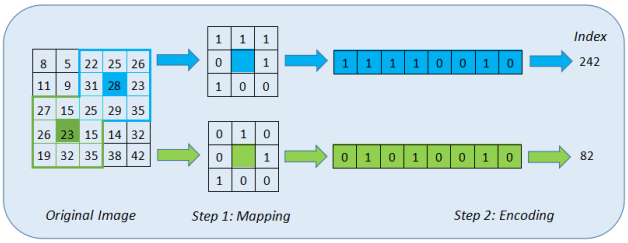

FIGURE 3. Illustrator of LBP feature: each pixel of the original image is first mapped into a binary string and then represented using a decimal number.

and its variants have been widely used for the steel surface defect classification task [3], [24].

B. MANIFOLD LEARNING

Most of the previous works on manifold learning devote to achieving the low-dimensional, compact representations of the given high-dimensional data which lies on or nearly on a manifold in unsupervised fashion. According to the learning objective, the related works of manifold learning can fall into two categories: transductive algorithms and the non-transductive algorithms. The transductive algorithms haven't the explicit mapping functions while learning the low-dimensional representations, such as Isomap [25], locally linear embedding [26], and Laplacian Eigenmap [27]. Normally, these algorithms can only achieve the low-dimensional representations of the given/training data points and be conducted by preserving the certain local or global properties of the manifold structure. On the contrary, the non-transductive algorithms are with the explicit mapping functions for the whole data space. Hence, these algorithms can achieve the low-dimensional representation of the new sample which doesn't exist in the training set. In this paper, the manifold structure is motivated from the study [25] which has declared that local linearity property holds everywhere on a global nonlinear manifold, and thus manifold can be modeled by a collection of local linear subspaces. Diverse from the previous local linear model [28] which involves the clustering algorithm, this work employs a flexible mechanism to generate the local model (LM) on the manifold by employing the distances defined in the literature [25].

Given the data set $X \in R^{L\times n}$, where L is the dimension and n is the number of the data points, it is expected to assume that all the data points come from a low-dimensional manifold $\mathcal{M}$. Therefore, the manifold learning is converted to search for a number of LMs. Suppose there are N local models and denote one of the LMs by C_i, we have

$$\begin{aligned} X &= C_1 \cup C_2 \cup \cdots \cup C_i \cup \cdots \cup C_N, \\ C_i \cap C_j &= \varnothing (i \neq j, i, j = 1, 2, \cdots, N), \\ C_i &= \{x_1^{(i)}, x_2^{(i)}, \cdots, x_{n_i}^{(i)}\}, \quad \sum_{i=1}^{N} n_i = n. \end{aligned} \tag{1}$$

From the property of LM formulated in (1), it can be seen that the original data points, e.g. DPDVs of the defect image, can be partitioned into some non-overlapped sets. As for the construction scheme, the LMs can be derived from X by utilizing the Euclidean distance matrix and geodesic distance matrix defined in [25]. The manifold represented using these LMs can well formulate the whole data points for the next pattern analysis applications.

III. DISCRIMINANT MANIFOLD REGULARIZED LOCAL DESCRIPTOR FOR STEEL SURFACE DEFECT CLASSIFICATION

The steel surface defect classification task aims at achieving the category of the defect by extracting the distinguishable feature and designing the proper classifier. In this section, the motivation is specified, and then the proposed algorithm for steel surface defect classification is presented in detail.

A. MOTIVATION

As discussed above, the local descriptor is commonly used as the feature description of the unconstrained image classification, e.g. the texture image, typically, the industry surface defect image. However, the previous local descriptor, such as LBP, HOG, and SIFT, involve the threshold operator and the hand-crafted definition as well as have the limitations of applications. In this paper, the proposed DMRLD describes the feature of the defect image based on the learning mechanism from a new sprite of view. The core idea of the proposed DMRLD lies in employing the learning strategy to construct the local information and preserve the raw, discriminant, and intrinsic structure of the defect image.

The proposed DMRLD algorithm for steel surface defect classification is outlined in Fig. 4. As shown in Fig. 4, there are three steps for the training procedure of DMRLD. Firstly, the DPDV associated with each pixel of the defect image is computed. Secondly, the manifold of the defect image is constructed by searching for a number of LMs spanned by these DPDVs. In the end, the projection is derived from the discriminant manifold learning to draw the low-dimensional subspace in which the discriminant property of the feature is enhanced for classification. Different from the previous local descriptors which extract the local information and generate the representation of the whole image, the proposed algorithm employs the manifold structure to regularize the local descriptor for representing the feature of the image. In order to boost the discriminant property of feature, manifold discriminant learning is conducted to learn the projection. Therefore, the format of the previous local descriptors is a vector, while the proposed DMRLD is in form of manifold.

B. IMPLEMENTATION OF DMRLD

The proposed DMRLD attempts to search for the manifold of the defect image in terms of LMs spanned by the DPDVs. According to the motivation specified above, the first step of DMRLD computes the DPDV associated with each pixel of the defect image. In the first step of the DMRLD approach,

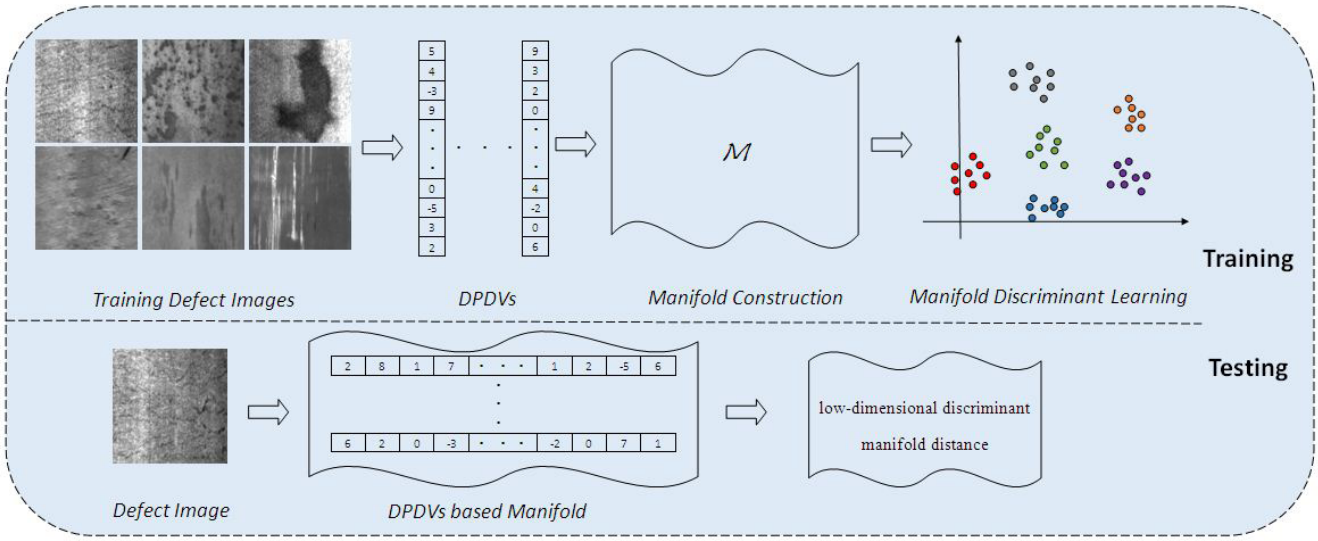

FIGURE 4. The training defect images are firstly represented using the DPDVs, and then the manifolds of these DPDVs are constructed to measure the features of the defect images. At last, the manifold discriminant learning is conducted to draw the projection. At the testing phase, the given new defect image is represented using the projected manifold structure, and the label can be determined using the manifold distance.

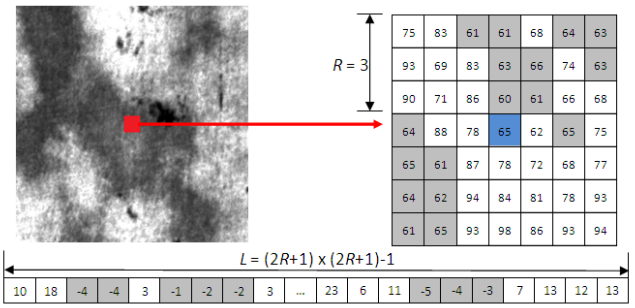

FIGURE 5. Computation of the 48-dimensional DPDV associated with the central pixel colored in blue, where the radius is set as 3.

each pixel is treated by computing the DPDV. The computation of DPDV associated with the pixel is illustrated in Fig. 5. From the construction of the DPDVs, it can be verified that the dimension $L = (2R + 1) * (2R + 1) - 1$, where R is the radius of the window. Compared with the original gray value, the DPDV describes the difference between the central pixel of the window and the neighboring pixels. Thus, DPDV can better reflect the spatial change of the pixel and encode the significant visual patterns implicitly, e.g. edges and lines in the image.

According to the DPDVs derived from the first step above, a collection of these DPDVs belonging to one image can be formulated as $X = [x_1, x_2, \cdots, x_i, \cdots, x_n]$, where x_i denotes the DPDV of the i-th pixel and n is the number of pixels in the image. As aforementioned, the DPDVs in the collection are expected to come from a low-dimensional manifold $\mathcal{M}$. Next, it is assumed that the manifold can be constructed using some LMs. Suppose we aim to partition the manifold into m LMs, and each LM is represented as C_j as introduced before. Based on the definition of LM, each LM can be constructed using the DPDVs. Given a pair of DPDVs x_i and x_j, they belong to the same LM only if $x_i \in \mathrm{KNN}(x_j)$ and $D_G(x_i, x_j) \leqslant \eta D_E(x_i, x_j)$, where $\mathrm{KNN}(x_j)$ indicates the set collected using the K nearest neighbors of x_j, and η is a threshold parameter and indicates the degree of linear perturbation of LM. Furthermore, D_G and D_E are the geometric and Euclidean distance defined in [25], where $D_E(x_i, x_j) = ||x_i - x_j||$ and $D_G(x_i, x_j)$ is computed via the two steps expressed in (2). From the generation of D_G, it can be seen that the first step initializes the value of each element and the second step refine the value by introducing the comparison criterion.

After initializing $D_G(x_i, x_j)$ by employing $D_E(x_i, x_j)$, the geodesic distance $D_G(x_i, x_j)$ is updated by computing the distance of nearest connected path between x_i and x_j, e.g.for each x_k, the sum of distances between x_i and x_k and that between x_j and x_k is compared with the original $D_G(x_i, x_j)$, and then the final value $D_G(x_i, x_j)$ is replaced with the smaller one. Actually, Step 2 searches for the shortest path of D_G and can be implemented using the famous Dijkstra algorithm. From the definition of LM, it can be observed that a larger η leads to fewer LMs but larger linear deviation, and vice versa. Hence, η controls the tradeoff between efficiency and accuracy. By initializing c seed points and integrating the pairs of DPDVs which meet the requirement expressed in (1), the LMs can be constructed to represent the manifold of the image. The procedure of constructing the LMs using the DPDVs is outlined in Algorithm 1.

$$\text{Step 1: } D_G(x_i, x_j) = \begin{cases} D_E(x_i, x_j), & \text{if } x_i \text{ is one of the } K \text{ nearest neighbors of } x_j, \text{ or vice versa.} \\ \infty, & \text{otherwise.} \end{cases}$$
$$\text{Step 2: For each } x_k \text{ in turn, replace all elements } D_G(x_i, x_j) = \min\{D_G(x_i, x_j), D_G(x_i, x_k) + D_G(x_k, x_j)\}. \quad (2)$$

Algorithm 1: Construction of the Local Model Using the DPDVs

Input: The collection of DPDVs X, parameter η.
Output: Local models X_C

Initialize $i = 1$, $C_i = \varnothing$, $X_C = \varnothing$, $X_T = X$;
While $X_T \neq \varnothing$ **do**:
    Randomly select a seed point from X_T as $x_1^{(i)}$, update $C_i = x_1^{(i)}$, $X_T = X_T - x_1^{(i)}$.
    For any $x_m^{(i)}$ and $x_n^{(i)} \in C_i$:
    If x_c is one of the K nearest neighbors of $x_m^{(i)}$, $x_c \in X_T$, and $D_G(x_c, x_n^{(i)})/D_E(x_c, x_n^{(i)}) < \eta$,
    Update $C_i = C_i \cup x_c$, $X_T = X_T - x_c$.
    If there is no x_cs can be added into C_i, then go to **Return**.
end while;
Return: $X_C = C_1 \cup C_2 \cup \cdots \cup C_i$, $X_T = X - X_C$.

C. DISCRIMINANT ANALYSIS ON THE MANIFOLD

According to Algorithm 1, the manifold in terms of the LMs using the DPDVs first extracts the local information and then constructs the manifold utilizing the LMs. Due to the linear property of the LMs, there exists redundant information. Thus, the discriminant learning is conducted on the manifold in this subsection to learn the projection.

Generally, it attempts to learn a projection which could map the original data into a low dimensional subspace in which the discriminant information of the data can be explored for the classification task [29], [30]. Given the LMs computed before, it is expected to learn the projection matrix $P \in R^{L\times d}$, where $d < L$. Then, the projected data in the same class should be close to each other and those from different classes are far from each other. To achieve the goal, we define two scatter terms S_w and S_b as follows:

$$S_w = \sum_{i,j} ||P^T x_i - P^T x_j||^2 W_{i,j} = 2P^T X(D - W)X^T P,$$
$$S_b = \sum_{i,j} ||P^T x_i - P^T x_j||^2 \hat{W}_{i,j} = 2P^T X(\hat{D} - \hat{W})X^T P, \quad (3)$$

where S_w and S_b characterize within-class compactness and between-class separability respectively, D and $\hat{D}$ are the diagonal matrices of W and $\hat{W}$, $D_{i,i} = \sum_j W_{i,j}$, $\hat{D}_{i,i} = \sum_j \hat{W}_{i,j}$. Furthermore, W and $\hat{W}$ are the affinity matrices of the intrinsic and penalty graphs, respectively. . It should be noticed that the non-zero weight in W and $\hat{W}$ should satisfy the base requirement that x_i is one of the K nearest neighbors of x_j or vice versa. Then, the corresponding elements can be computed via:

$$W_{i,j} = \begin{cases} \exp(\frac{-||x_i - x_j||^2}{t}), & \delta(x_i) = \delta(x_j) \\ 0, & \text{otherwise} \end{cases}$$
$$\hat{W}_{i,j} = \begin{cases} \exp(\frac{-||x_i - x_j||^2}{t}), & \delta(x_i) \neq \delta(x_j) \\ 0, & \text{otherwise} \end{cases} \quad (4)$$

where $\delta(\cdot)$ indicates the class label and t is the kernel width. From the definition of the affinity matrix, it can be observed that the neighboring LMs of the manifolds belonging to the same training class will not be allowed to be connected in the penalty graph. In order to learn the discriminant projection, the following problem is expected to be solved by maximizing the objective:

$$\max \frac{P^T X(\hat{D} - \hat{W})X^T P}{P^T X(D - W)X^T P} \quad (5)$$

It can be observed that the projection P can be constructed using eigenvectors corresponding to the top d largest eigenvalues in $P^T X(\hat{D} - \hat{W})X^T P = \lambda P^T X(D - W)X^T P$, where λ is the eigenvalue. Since the discriminant projection P can extract the distinguishable feature for classification, the LMs can be represented using the projected DPDVs before conducting the classification task.

D. DMRLD FOR STEEL SURFACE DEFECT CLASSIFICATION

In the previous local descriptor works, the descriptor matching is conducted for the classification task using the commonly-used nearest neighbor classifier. However, this work represents the feature of the defect image in terms of local descriptor by utilizing the structure of manifold, a collection of LMs. Therefore, it is expected to match the manifolds belonging to different defect images.

Similar to the nearest neighbor classifier which adopts the Euclidean distance, cosine values and other vector-based metrics, the distance between one manifold and another is expected to measure the similarity of two defect images in this work. There have been developed numerous manifold metric learning works in recent years. The definition of the distance can be categorized into variation based and exemplar based measure.

According to the canonical vectors defined in [31], we can introduce the variation based distance as follows:

$$d_V(C_i, C_j) = \frac{r}{\sum_{k=1}^{r} \lambda_k}, \quad (6)$$

where λ_k is the k-th largest singular value by conducting singular vector decomposition to $Z_i^T Z_j$, and Z_i and Z_j are the orthogonal basis of the two subspaces C_i and C_j, respectively. The measurement in terms of $d_V(C_i, C_j)$ takes into account the common variation of the DPDVs in the two defect images.

In addition, the appearance of these DPDVs in the two defect images should also be involved into the proposed distance. Denote the mean vectors of the two defect images by e_i and e_j. Then, we define the exemplar distance as follows:

$$d_E(C_i, C_j) = \frac{||e_i|| \cdot ||e_j||}{e_i^T e_j}. \quad (7)$$

By integrating the two measurements into the final distance, we can obtain the weighted distance as follows:

$$d(C_i, C_j) = \alpha \cdot d_V(C_i, C_j) + (1 - \alpha) \cdot d_E(C_i, C_j) \quad (8)$$

where α is the weight parameter to keep the balance between the two measurements. According to the distance computed using these subspaces from the manifolds, it can determine the similarity of the manifolds. The defect image classification procedure using the proposed DMRLD algorithm is outlined in Algorithm 2.

E. DISCUSSION

This work aims at learning the representation of the defect image using the discriminant manifold regularized local descriptor. Different from the previous local descriptor works, the proposed algorithm devotes to adopting the learning mechanism rather than the hand-crafted manner. Correspondingly, the distance of the two defect images is converted to the distance between the subspaces.

Compared with the previous local descriptor, the proposed DMRLD also has to compute the local difference-like information, e.g. DPDVs. Then, each defect image can be represented employing Algorithm 1 acting on these DPDVs in form of LMs. Another difference lies in that an integrated measurement is introduced into this paper for completely learning the manifold metric. From the view of feature extraction, the previous local descriptor is denoted by a vector while the proposed algorithm represent the feature using a number of LMs. Furthermore, the proposed DMRLD derives the discriminant representation from the manifold discriminant analysis to achieve the low-dimensional manifold representation which assists in classification.

In summary, the proposed DRMLD algorithm employ the pixel difference information and incorporates the discriminate learning mechanism into the descriptor. The characteristics of the common local descriptors are outlined in Table 2. The related local descriptors are computed via the structure of region, such as HOG divides the image via some cells and blocks, or pixel-based structure, such as others including the proposed DRMLD in which the descriptors are computed using the neighborhoods of central pixel. In addition, both HOG and SIFT determine the descriptor in terms of gradient, while only the proposed DMRLD introduces the learning mechanism without employing the histogram format.

TABLE 2. Characteristics of the related local descriptors.

Method	Structure	Gradient	Histogram	Learning
HOG	Region	$\surd$	$\surd$	$\times$
SIFT	Pixel	$\surd$	$\surd$	$\times$
LBP	Pixel	$\times$	$\surd$	$\times$
CLBP	Pixel	$\times$	$\surd$	$\times$
AECLBP	Pixel	$\times$	$\surd$	$\times$
DMRLD	Pixel	$\times$	$\times$	$\surd$

IV. EXPERIMENT AND ANALYSIS

The proposed local descriptor employs the manifold structure to extract the local information of the defect image. In this section, the experiments on the steel surface defect image dataset are conducted to verify the performance of the proposed DMRLD algorithm, and then the experiments on the Kylberg texture dataset are conducted to illustrate the texture descriptor ability of the proposed DMRLD algorithm.

A. EXPERIMENT SETTINGS

In order to verify the performance of the proposed algorithm, the famous local descriptor, such as LBP [18] and the variants CLBP [24] and AECLBP [3], HOG [19], and SIFT [20], are used for comparison. By computing the local binary coding in a 3×3 window, each image is represented as a 256-dimensional vector. As for HOG descriptor, there are four parameters in total, cell size, block size, number of overlapping, and number of bins. Considering the structure of HOG, we tune the size of cell from 8×8 to 128×128 on the steel surface defect dataset and 8×8 to 256×256 on the Kylberg texture dataset, respectively. In the applications, the number of bins is set as 9 in default, the block size is set as [22] which indicates there are 2×2 cells construct one block, and the overlapping is set as $blocksize/2$. Then, we run HOG based classification algorithm and select the cell size for the best classification accuracy. In this experiment, the cell size of HOG is set as 64×64 and generate 324-dimensional feature descriptors on the NEU steel surface defect dataset. The cell size of HOG corresponding to the best classification accuracy on the Kylberg dataset is set as 128×128, then each image is represented as a 324-dimensional vector. Due to the distance employed in the proposed algorithm, the nearest neighbors classifier is utilized in the experiment. All the algorithms are implemented on the platform of Matlab 2014a and Intel Core i5-4460 3.20GHz 8GB memory.

B. EXPERIMENTS ON THE STEEL SURFACE DEFECT IMAGE DATASET

In this subsection, we construct the experiments on the NEU steel surface defect dataset across six types of defects, i.e., crazing (Cr), inclusion (In), patches (Pa), pitted surface (PS), rolled-in scale (RS), and scratches (Sc), includes 1800 gray scale images: 300 samples each of six different kinds of typical surface defects. Fig. 6 shows the example images of six types of surface defects, and each image is

Algorithm 2: Manifold Regularized Local Descriptor for Steel Surface Defect Classification

Input: The training defect images X and the testing defect image y.
Output: Defect category of y.
1 **Step 1:** Obtain the manifolds of training defect images and the testing defect image in terms of LMs using Algorithm 1.
2 **Step 2:** Compute the scatter matrices S_w and S_b via (3).
3 **Step 3:** Learn the projection P by solving the problem (5).
4 **Step 4:** Compute the distance from manifold to manifold according to the fused distance in (8).
5 **Step 5:** Defect category of y can be determined by $l_y = \arg\min d(P^T C_i, P^T C_j)$, where C_i is one of the LMs from the testing defect image and C_j is one of the LMs from the training defect image.

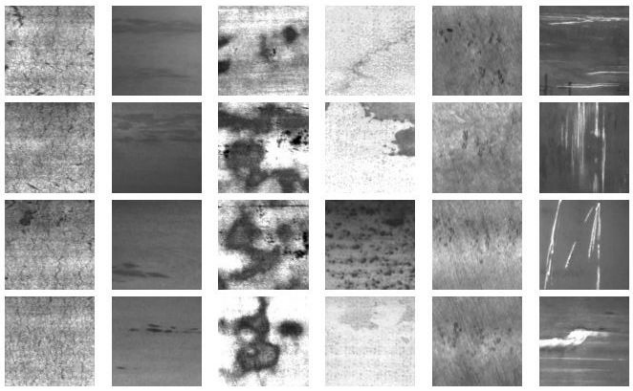

FIGURE 6. Example defect images of the NEU steel surface defect dataset.

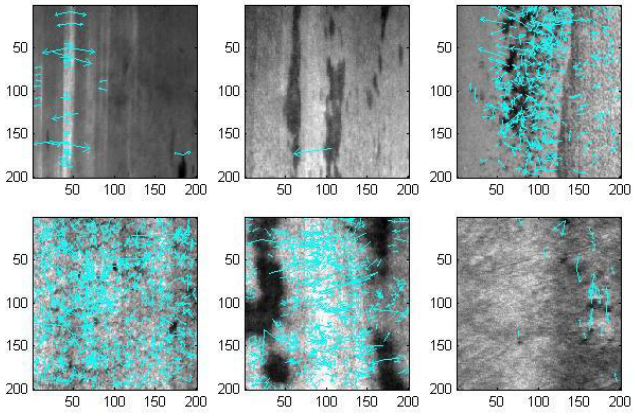

FIGURE 7. SIFT feature visualization of some defect images of the strip steep surface. Defect category from left column to right column: crazing, inclusion, patches, pitted surface, rolled-in scale, and scratches.

normalized into 300 × 300 pixels according to [3]. From Fig. 6, it can be seen that the defects are several of shapes and sizes, such as patches, pitted surface, and scratches.

Before evaluating the performance of the proposed algorithm, we show the SIFT key points on the defect images in Fig. 7 as well. The steel surface is too coarse to capture the discriminant feature using SIFT descriptors. From the visualization of the key points detected using SIFT method, it can be observed that the numbers of key points across different sorts of defects vary largely.

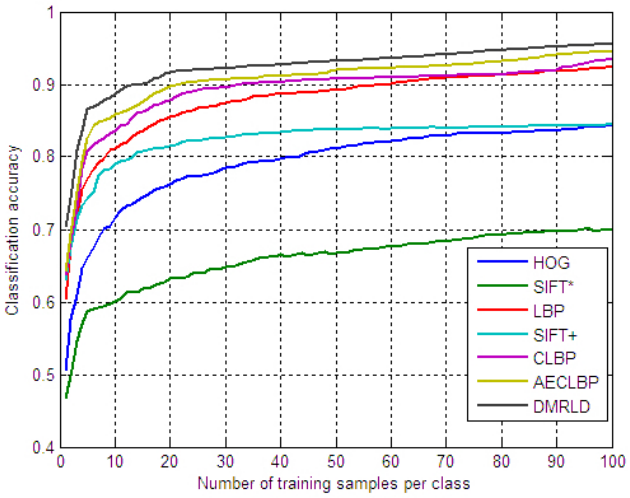

FIGURE 8. Classification accuracies of the competitive algorithms versus the number of training images on the strip steel surface defect dataset.

Considering the extreme case in which no key points are detected in the defect image, the classification task using SIFT cannot be accomplished. The classification results in terms of mean and standard deviation by ten repeated experiments on the steel strip defect dataset are reported in Table 3. For completely reporting the classification results, the number of images for each class ptr varies from 1 to 7 to construct the training set. Due to the complex patterns of the defects, $\eta = 0.8$ and the number of nearest neighbors is set as 3 while searching for the subspaces. Meanwhile, the kernel width t is set as 2 and $\alpha = 0.7$. From Table 3, it can be observed that SIFT based methods cannot achieve the comparable results among the competitive methods, which responses to the visualization of the key points in the defect images. With the increasing of the number of training images, the classification results improve gradually. Among the compared methods, the LBP variants including CLBP and AECLBP obtain the second tier best results. Without the requirement of the key points, the proposed DMRLD still achieves the best classification result.

The classification results of the competitive methods versus the number of training defect images per class are shown in Fig. 8. From Fig. 8, we can find that SIFT with maximum operation achieves the worst classification result among the

TABLE 3. Classification accuracies (Mean±Std.)% on the strip steel defect dataset.

Algorithm	$ptr = 1$	$ptr = 2$	$ptr = 3$	$ptr = 4$	$ptr = 5$	$ptr = 6$	$ptr = 7$
HOG	50.51 ± 4.27	57.70 ± 3.86	60.98 ± 3.83	64.57 ± 3.44	66.12 ± 3.56	67.51 ± 3.03	68.94 ± 3.11
SIFT+	62.84 ± 4.67	67.37 ± 3.33	71.46 ± 2.55	73.28 ± 3.11	74.23 ± 2.80	75.13 ± 2.89	77.53 ± 2.12
SIFT*	46.68 ± 7.15	49.81 ± 4.18	54.58 ± 2.91	56.89 ± 2.39	58.60 ± 2.75	59.04 ± 2.05	59.23 ± 1.93
LBP	60.21 ± 4.72	67.65 ± 4.68	71.67 ± 3.30	75.61 ± 2.47	76.97 ± 2.12	78.39 ± 1.93	79.27 ± 2.00
CLBP	63.63 ± 5.23	68.26 ± 4.23	73.08 ± 2.75	78.52 ± 3.07	80.75 ± 2.91	81.68 ± 3.22	82.16 ± 2.27
AECLBP	64.06 ± 4.77	69.38 ± 3.72	75.11 ± 2.52	79.32 ± 3.26	82.62 ± 2.69	84.36 ± 2.21	84.86 ± 2.40
DMRLD	70.35 ± 4.35	74.23 ± 3.81	80.89 ± 2.63	83.63 ± 2.62	86.52 ± 2.06	87.01 ± 1.80	87.36 ± 2.03

TABLE 4. Classification accuracies (Mean±Std.)% versus α on the NEU steel surface defect dataset.

α	$ptr = 1$	$ptr = 2$	$ptr = 3$	$ptr = 4$	$ptr = 5$	$ptr = 6$	$ptr = 7$
0.0	60.68 ± 3.96	64.86 ± 4.03	69.60 ± 2.39	72.99 ± 2.44	74.75 ± 1.56	78.21 ± 2.86	80.65 ± 1.86
0.1	64.21 ± 4.01	67.68 ± 3.96	75.49 ± 2.52	78.22 ± 3.02	79.03 ± 2.74	81.67 ± 2.55	83.05 ± 1.88
0.2	66.37 ± 3.88	69.35 ± 2.77	75.46 ± 1.95	77.38 ± 2.21	81.19 ± 1.76	84.93 ± 1.32	85.53 ± 2.33
0.3	66.52 ± 3.63	69.05 ± 3.55	77.86 ± 2.48	79.42 ± 1.32	82.35 ± 2.23	85.56 ± 1.82	85.78 ± 2.06
0.4	67.35 ± 4.17	70.21 ± 4.05	79.12 ± 2.44	78.36 ± 1.57	82.55 ± 2.37	86.98 ± 2.19	87.42 ± 1.45
0.5	70.35 ± 4.35	74.23 ± 3.81	80.89 ± 2.63	83.63 ± 2.62	86.52 ± 2.06	87.01 ± 1.80	87.36 ± 2.03
0.6	72.13 ± 4.04	73.53 ± 3.53	79.72 ± 2.49	80.58 ± 2.42	82.26 ± 1.83	86.12 ± 2.08	88.04 ± 2.85
0.7	71.01 ± 3.65	73.12 ± 3.62	77.65 ± 3.01	78.89 ± 2.00	83.33 ± 2.84	85.63 ± 2.34	87.22 ± 2.55
0.8	70.70 ± 4.88	71.03 ± 3.76	73.83 ± 2.38	75.23 ± 2.77	79.12 ± 2.31	81.59 ± 2.80	84.19 ± 2.62
0.9	69.98 ± 5.02	70.58 ± 4.29	71.14 ± 2.59	73.01 ± 3.26	76.59 ± 2.44	80.05 ± 2.71	82.26 ± 2.37
1.0	68.82 ± 4.77	68.59 ± 3.86	70.92 ± 2.79	72.27 ± 2.87	75.81 ± 3.06	80.83 ± 2.08	81.19 ± 2.74

compared methods. Since the keypoints are unreliable on the real steel surface defect images, the performance of SIFT based methods degrade obviously.

In addition, the weight α in the fused manifold distance determines the importances of the two metrics. In order to follow the classification accuracy versus α, we report the experimental results versus different settings of α in Table 4. From Table 4, it can be observed that bigger alpha assists in achieving the higher classification accuracy. From the fused distance, alpha indicates the weight of the variation based distance. From Table 4, it can also be observed that the classification accuracies when $\alpha = 0$ and $\alpha = 1$ are relatively worse than those of other settings. Therefore, the fused mechanism works for the manifold metric. Exactly, the variation distance ($\alpha = 1.0$) plays more important role than exemplar distance ($\alpha = 0$) in manifold metric learning.

In order to illustrate the analysis on this point, the confused matrix based on the classification results using the compared methods is presented in Fig. 9. By comparing the classification results versus the category, it can be observed that the classification results on the defect labeled 'inclusion' are heavily worse than those on the other category while using SIFT based methods. Furthermore, the classes named 'pitted surface' and 'scratches' confront the case that few keypoints are available for generating the descriptors. By counting the results using SIFT based methods, it can be found that there are 64%, 5%, and 2% images lacking of keypoints for the class 'inclusion', 'pitted surface', and 'scratches', respectively. Therefore, it can also illustrate that it has a high requirement of the image to utilize the SIFT descriptor. Meanwhile, the proposed DMRLD method is robust to texture image as well as the real steel surface defect image.

C. EXPERIMENTS ON THE KYLBERG TEXTURE DATASET

In this paper, the proposed DMRLD is designed for extracting the discriminant yet completed local feature for steel surface defect classification. However, the proposed DMRLD should work for the normal texture feature. For this, we employ the

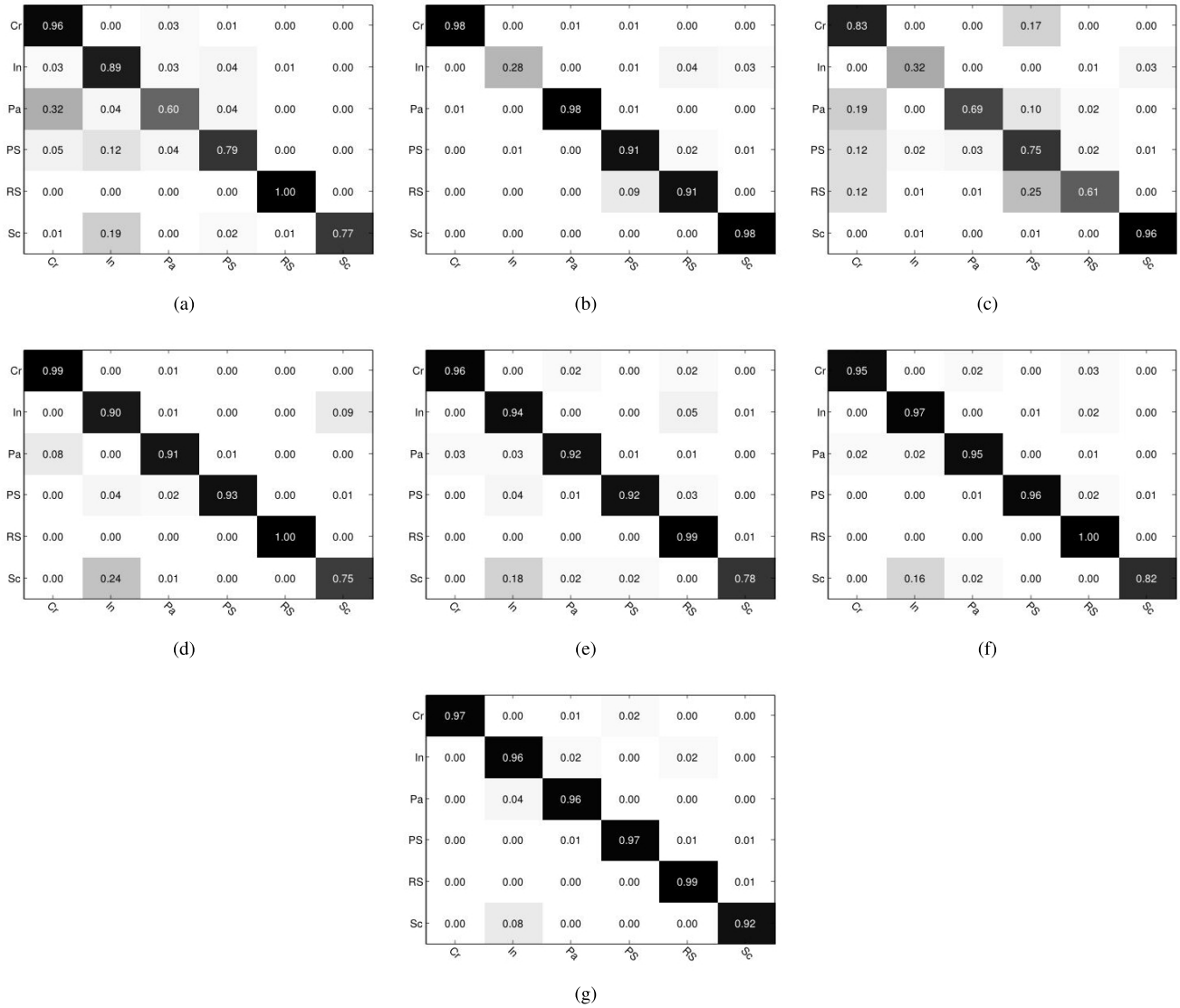

FIGURE 9. Confused matrices by using the compared methods (a) HOG, (b) SIFT*, (c) SIFT+, (d) LBP, (e) CLBP, (f) AECLBP, and (g) DMRLD on the real steel surface defect dataset.

famous Kylberg texture dataset to conduct the experiments to evaluate the competitive methods. Kylberg texture dataset is widely-used for evaluating the performance on texture descriptors. Kylberg texture dataset [32] consists of 28 texture classes. There are 160 unique texture patches per class. The patch size of the texture is 576 × 576. All patches are normalized with a mean value of 127 and a standard deviation of 40. Some of the samples are shown in Fig. 10. In this experiment, a small subset of the dataset including 6 classes with 40 samples are employed for evaluating the performance of the competitive algorithms.

Since the variation of the appearance in the same class is not large on the Kylberg texture dataset, we randomly select 1, 2, and 3 samples per class to construct the training set and the rests are for testing. According to the property of the compared algorithms, the SIFT feature is computed using maximum and mean schemes on the whole 128-dimensional vectors. If the SIFT is derived by averaging the whole features

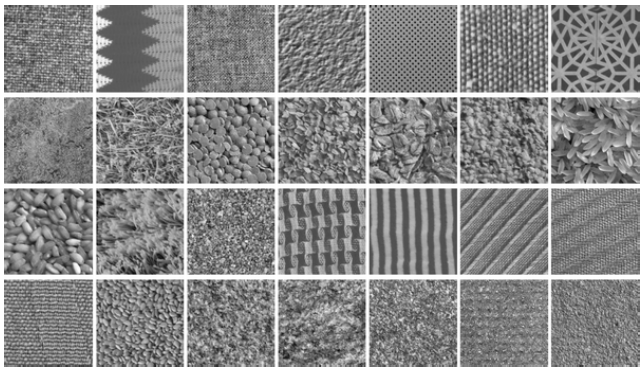

FIGURE 10. Example patches from each one of the 28 texture classes.

belonging to the image, we mark the corresponding algorithm as SIFT+, otherwise, SIFT*. Fig. 11 shows some of key points detected using SIFT on the Kylberg texture images.

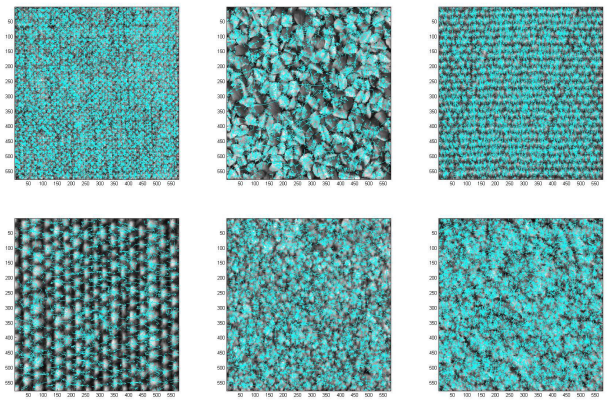

FIGURE 11. SIFT feature visualization of some patches on the Kylberg dataset.

TABLE 5. Classification accuracies (Mean±Std.)% on the kylberg texture dataset.

Algorithm	$ptr = 1$	$ptr = 2$	$ptr = 3$
HOG	40.60 ± 7.75	46.32 ± 5.13	49.64 ± 3.87
SIFT+	93.21 ± 3.75	96.84 ± 3.02	99.05 ± 1.68
SIFT*	70.04 ± 5.45	77.11 ± 4.52	81.85 ± 3.08
LBP	90.00 ± 5.22	96.18 ± 2.57	97.43 ± 1.60
CLBP	92.21 ± 4.89	95.68 ± 2.36	97.55 ± 1.88
AECLBP	92.63 ± 3.86	96.52 ± 2.33	97.86 ± 1.92
DMRLD	94.75 ± 3.25	97.67 ± 2.17	99.82 ± 1.68

It can be observed that there are dense points which correspond to the features.Different from the texture images on the Kylberg texture dataset, the real strip steel surface demonstrates various patterns and has a terrible quality.

As for the proposed MRLD algorithm, we set $\eta = 2$ and the number of nearest neighbors as 5 in Algorithm 1 for constructing the local models. During the learning process, the dimension of the projection $d = 10$ and the kernel width $t = 2$ in Eq. (4). At last, the fused distance defined in Eq. (10) is computed by setting $\alpha = 0.5$. The results in terms of mean and standard deviation by repeating the procedure for 10 times are reported in Table 5. From the classification results in Table 5, it can be seen that the proposed DMRLD performs better than other competitive algorithms. Among the compared algorithms, SIFT+ and SIFT* achieve the second tier best results due to the discriminant ability of feature measurement. At the same time, it can be checked from Fig. 11 that there are plenty of key points to support the discriminant feature descriptors while employing SIFT descriptors. Furthermore, the results of HOG performs worst among the compared methods due to the strict feature extraction on the edge rather than the texture.

Meanwhile, we show the classification accuracies of the competitive algorithms versus the number of training samples in Fig. 12. With plenty of training samples, the competitive algorithms can achieve the similar, promising results. It can be seen that the proposed DMRLD outperforms other methods in the case that there are small number of training samples in the training set. It illustrates that the proposed DMRLD takes the best result on the dataset while extracting the local information to represent the texture image.

TABLE 6. Computation time (ms) on the two datasets using the compared methods.

Method	Kylberg	NEU steel surface
HOG	33.6	7.18
SIFT+	3633.7	510.2
SIFT*	3638.6	511.3
LBP	34.2	5.79
CLBP	36.1	5.93
AECLBP	38.4	6.08
DMRLD	45.5	7.31

D. EXPERIMENT ANALYSIS AND DISCUSSION

From the experiment results on the Kylberg texture dataset and the NEU steel surface defect dataset, we can achieve the following observations:

1) The experiments on the Kylberg texture dataset illustrate the performance of the proposed DMRLD. With the increasing number of the training samples, the methods can achieve similar classification accuracy. Typically, both DMRLD and SIFT+ obtain 99%+. However, the proposed DMRLD still gets the best classification accuracy and improves 1.5% when $ptr = 1$ compared with SIFT+. In addition, DMRLD improves 2% + compared with LBP variants. Therefore, DMRLD can extract the texture descriptors on the normal texture images.

2) NEU steel surface defect dataset consists of sorts of defects. From the comparison, it can be observed that AECLBP obtains the second best classification accuracy. The proposed DMRLD improves about 5% than AECLBP with different numbers of training samples. Another interesting observations lies in that SIFT based methods fail to work for defect classification. Due to the number of key points, SIFT+ cannot achieve the similar results on the Kylberg dataset. Thus, DMRLD gets better than SIFT+ about 8%-10% in terms of classification accuracy.

Since the local descriptor is designed for steel surface defect image, the computation time is one of the key issues during the application. Thus, we report the computation time of classifying one defect image by employing the competitive methods in Table 6. From Table 6, it can be observed that the SIFT based methods take more time in classifying the image than other compared ones due to the keypoints detection. The

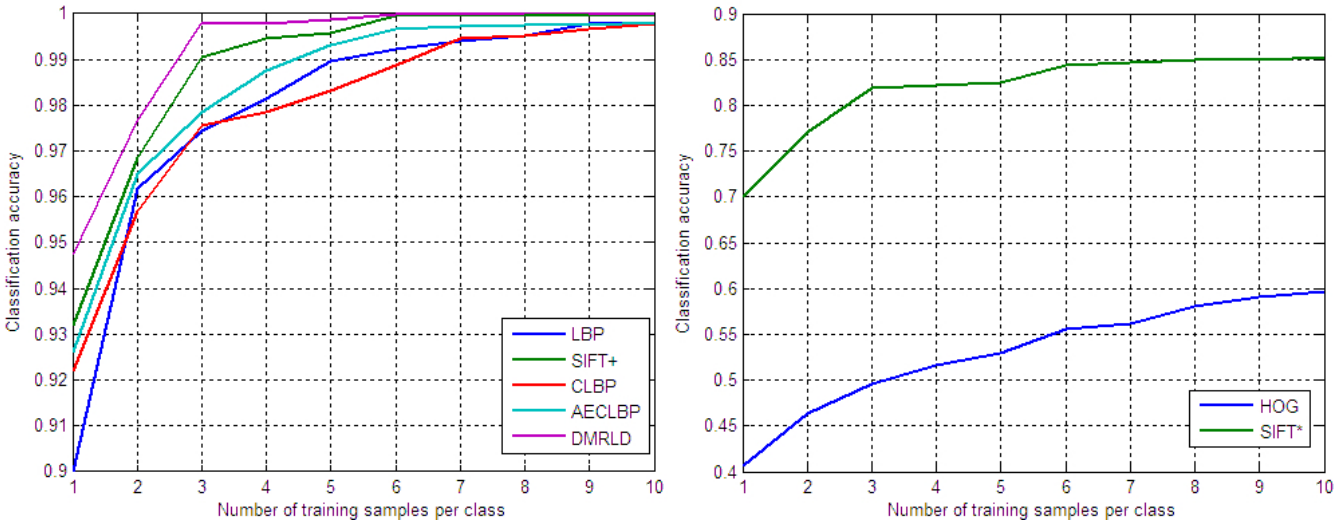

FIGURE 12. Classification accuracies of the competitive algorithms versus the number of training samples on the Kylberg texture dataset.

original LBP is more efficient than any other methods in the classification task. Furthermore, the proposed DMRLD gets the similar computation time with the LBP variants during the experiment yet achieves the best classification accuracy. According to the related production, the COGNEX inspection production allows 2.1−2.6 meters per second for the craft speed. From Table 6, it can be seen that the proposed DMLRD algorithm can conduct 7000+ rounds classification task per second. Therefore, the proposed DMRLD can be qualified to the defect classification task in the application.

V. CONCLUSION

A new approach to the local descriptor algorithm is proposed in this paper to solve the problem of steel surface defect image classification. Considering the previous local descriptors are constructed in hand-crafted fashion, the proposed method introduces the structure of manifold into learning the descriptors of the defect image. By defining the criterion as well as involving the learning mechanism, the local models in terms of DPDVs are achieved. Furthermore, the discriminant information is utilized into the dimension reduction processing to learn the projection. Finally, the integrated distance which simultaneously takes into account the variation and exemplar distances is given for measuring the similarity between the local models. Compared with the previous, famous local descriptors, the proposed DMRLD method can better capture the distinguishable feature without high requirement of the defect image quality. Therefore, the proposed method is more robust than the compared methods in the real steel surface defect classification. Experiments on the open Kylberg texture dataset illustrate that DMRLD outperforms SIFT descriptor which is the best compared method. Moreover, the experiments on the real steel surface defect dataset show the effectiveness and robustness of DMRLD. Due to the performance of DMRLD, it will be employed to guide the defect detection in the future work.

REFERENCES

[1] H. Jia, L. M. Yi, J. Shi, and T. S. Chang, "An intelligent real-time vision system for surface defect detection," in *Proc. Int. Conf. Pattern Recognit.*, vol. 3, 2004, pp. 239–242.
[2] S. Ghorai, A. Mukherjee, M. Gangadaran, and P. K. Dutta, "Automatic defect detection on hot-rolled flat steel products," *IEEE Trans. Instrum. Meas.*, vol. 62, no. 3, pp. 612–621, Mar. 2013.
[3] K. Song and Y. Yan, "A noise robust method based on completed local binary patterns for hot-rolled steel strip surface defects," *Appl. Surf. Sci.*, vol. 285, no. 21, pp. 858–864, Nov. 2013.
[4] H. Hua, Y. Liu, M. Liu, and L. Nie, "Surface defect classification in large-scale strip steel image collection via hybrid chromosome genetic algorithm," *Neurocomputing*, vol. 181, pp. 86–95, Mar. 2016.
[5] M. Chu, J. Zhao, X. Liu, and R. Gong, "Multi-class classification for steel surface defects based on machine learning with quantile hyper-spheres," *Chemometrics Intell. Lab. Syst.*, vol. 168, pp. 15–27, Sep. 2017.
[6] Y. J. Zhao, Y. H. Yan, and K. C. Song, "Vision-based automatic detection of steel surface defects in the cold rolling process: Considering the influence of industrial liquids and surface textures," *Int. J. Adv. Manuf. Technol.*, vol. 90, nos. 5–8, pp. 1–14, 2016.
[7] W. Zhu, Y. Yan, and Y. Peng, "Pair of projections based on sparse consistence with applications to efficient face recognition," *Signal Process., Image Commun.*, vol. 55, pp. 32–40, 2017.
[8] W. Zhu and Y. Yan, "Joint linear regression and nonnegative matrix factorization based on self-organized graph for image clustering and classification," *IEEE Access*, vol. 6, pp. 38820–38834, 2018.
[9] C. S. Lee, C.-H. Choi, J. Y. Choi, Y. K. Kim, and S. H. Choi, "Feature extraction algorithm based on adaptive wavelet packet for surface defect classification," in *Proc. Int. Conf. Image Process.*, vol. 2, 1996, pp. 673–676.
[10] C. Dongyan, X. Kewen, N. Aslam, and H. Jingzhong, "Defect classification recognition on strip steel surface using second-order cone programming-relevance vector machine algorithm," *J. Comput. Theor. Nanosci.*, vol. 13, no. 9, pp. 6141–6148, 2016.
[11] M. Chu, R. Gong, and A. Wang, "Strip steel surface defect classification method based on enhanced twin support vector machine," *Trans. Iron Steel Inst. Jpn.*, vol. 54, no. 1, pp. 119–124, 2014.
[12] H. Hasni, A. H. Alavi, P. Jiao, and N. Lajnef, "Detection of fatigue cracking in steel bridge girders: A support vector machine approach," *Archives Civil Mech. Eng.*, vol. 17, no. 3, pp. 609–622, 2017.

[13] G. H. Fu, B. Y. Zhang, H. D. Kou, and L. Z. Yi, "Stable biomarker screening and classification by subsampling-based sparse regularization coupled with support vector machines in metabolomics," *Chemometrics Intell. Lab. Syst.*, vol. 160, pp. 22–31, Jan. 2017.
[14] M. R. Halfawy and J. Hengmeechai, "Automated defect detection in sewer closed circuit television images using histograms of oriented gradients and support vector machine," *Autom. Construct.*, vol. 38, no. 5, pp. 1–13, 2014.
[15] W. Wu and H. Zhou, "Data-driven diagnosis of cervical cancer with support vector machine-based approaches," *IEEE Access*, vol. 5, pp. 25189–25195, 2017.
[16] F. Mekhalfa and N. Nacereddine, "Multiclass classification of weld defects in radiographic images based on support vector machines," in *Proc. 10th Int. Conf. Signal-Image Technol. Internet-Based Syst.*, 2014, pp. 1–6.
[17] M. Chu, R. Gong, S. Gao, and J. Zhao, "Steel surface defects recognition based on multi-type statistical features and enhanced twin support vector machine," *Chemometrics Intell. Lab. Syst.*, vol. 171, pp. 140–150, Dec. 2017.
[18] T. Ojala, M. Pietikäinen, and T. Mäenpää, "Multiresolution gray-scale and rotation invariant texture classification with local binary patterns," *IEEE Trans. Pattern Anal. Mach. Intell.*, vol. 24, no. 7, pp. 971–987, Jul. 2002.
[19] N. Dalal and B. Triggs, "Histograms of oriented gradients for human detection," in *Proc. IEEE Conf. Comput. Vis. Pattern Recognit.*, Jun. 2005, pp. 886–893.
[20] D. G. Lowe, "Distinctive image features from scale-invariant keypoints," *Int. J. Comput. Vis.*, vol. 60, no. 2, pp. 91–110, 2004.
[21] C. H. Chan, J. Kittler, and K. Messer, "Multi-scale local binary pattern histograms for face recognition," in *Proc. Int. Conf. Adv. Biometrics*, 2007, pp. 809–818.
[22] B. Zhang, Y. Gao, S. Zhao, and J. Liu, "Local derivative pattern versus local binary pattern: Face recognition with high-order local pattern descriptor," *IEEE Trans. Image Process.*, vol. 19, no. 2, pp. 533–544, Feb. 2010.
[23] C. Chen, M. Liu, H. Liu, B. Zhang, J. Han, and N. Kehtarnavaz, "Multi-temporal depth motion maps-based local binary patterns for 3-d human action recognition," *IEEE Access*, vol. 5, pp. 22590–22604, 2017.
[24] Z. Guo, L. Zhang, and D. Zhang, "A completed modeling of local binary pattern operator for texture classification," *IEEE Trans. Image Process.*, vol. 19, no. 6, pp. 1657–1663, Jun. 2010.
[25] J. B. Tenenbaum, V. de Silva, and J. C. Langford, "A global geometric framework for nonlinear dimensionality reduction," *Science*, vol. 290, no. 5500, pp. 2319–2323, Dec. 2000.
[26] S. T. Roweis and L. K. Saul, "Nonlinear dimensionality reduction by locally linear embedding," *Science*, vol. 290, no. 5500, pp. 2323–2326, Dec. 2000.
[27] M. Belkin and P. Niyogi, "Laplacian eigenmaps and spectral techniques for embedding and clustering," in *Advances in Neural Information Processing System*, vol. 14. Cambridge, MA, USA: MIT Press, 2002, pp. 585–591.
[28] T. K. Kim, O. Arandjelovic, and R. Cipolla, "Learning over sets using boosted manifold principal angles (BoMPA)," in *Proc. Brit. Mach. Vis. Conf.*, 2005, pp. 779–788.
[29] W. Zhu, Y. Yan, and Y. Peng, "Dictionary learning based on discriminative energy contribution for image classification," *Knowl.-Based Syst.*, vol. 113, pp. 116–124, Dec. 2016.
[30] W. Zhu and Y. Yan, "Label and orthogonality regularized non-negative matrix factorization for image classification," *Signal Process., Image Commun.*, vol. 62, pp. 139–148, Mar. 2018.
[31] A. Björck and G. H. Golub, "Numerical methods for computing angles between linear subspaces," *Math. Comput.*, vol. 27, no. 123, pp. 579–594, 1973.
[32] G. Kylberg, "The kylberg texture dataset v. 1.0," Centre Image Anal., Swedish Univ. Agricult. Sci., Uppsala Univ., Uppsala, Sweden, Tech. Rep. 35, Sep. 2011. [Online]. Available: http://www.cb.uu.se/~gustaf/texture/

JIULIANG ZHAO received the B.S. degree from the Wuhan Institute of Iron and Steel in 1988, and the M.S. degrees from the School of Mechanical Engineering and Automation, Northeastern University, Shenyang, China, in 2002, where he is currently pursuing the Ph.D. degree. His research interests include vision-based defect detection and recognition.

YISHU PENG received the B.S., M.S., and Ph.D. degrees from the School of Mechanical Engineering and Automation, Northeastern University, Shenyang, China, in 2009, 2011, and 2016, respectively. Since 2016, he has been a Teacher with the Hunan Institute of Science and Technology. His research interest covers steel surface defect analysis and pattern recognition.

YUNHUI YAN received the B.S., M.S., and Ph.D. degrees from the School of Mechanical Engineering and Automation, Northeastern University, Shenyang, China, in 1981, 1985, and 1997, respectively. He has been a Teacher with Northeastern University, since 1982, and became a Professor in 1997. From 1993 to 1994, he stayed at the Tohoku National Industrial Research Institute as a Visiting Scholar. His research interest covers intelligent inspection, image processing, and pattern recognition.